Submitted to Astrophys.J.

SLAC-PUB-12460

astro-ph/0612038

Draft version December 4, 2006

Preprint typeset using LaTeX style emulateapj v. 26/01/00

APPLICATION OF A XMM-NEWTON EPIC MONTE CARLO TO ANALYSIS AND INTERPRETATION OF DATA FOR ABELL 1689, RXJ0658-55 AND THE CENTAURUS CLUSTERS OF GALAXIES

K. Andersson[1,3], J.R. Peterson[2,4], G. Madejski[3,4]

[1] Stockholm University, S-106 91, Stockholm, Sweden

[2] Purdue University, West Lafayette, IN 47907, USA

[3] Stanford Linear Accelerator Center, Menlo Park, CA 94025, USA

[4] KIPAC, Stanford University, PO Box 20450, Stanford, CA 94309, USA

Draft version December 4, 2006

ABSTRACT

We propose a new Monte Carlo method to study extended X-ray sources with the European Photon Imaging Camera (EPIC) aboard XMM Newton. The Smoothed Particle Inference (SPI) technique, described in a companion paper, is applied here to the EPIC data for the clusters of galaxies Abell 1689, Centaurus and RXJ 0658-55 (the "bullet cluster"). We aim to show the advantages of this method of simultaneous spectral-spatial modeling over traditional X-ray spectral analysis. In Abell 1689 we confirm our earlier findings about structure in temperature distribution and produce a high resolution temperature map. We also confirm our findings about velocity structure within the gas. In the bullet cluster, RXJ 0658-55, we produce the highest resolution temperature map ever to be published of this cluster allowing us to trace what looks like the motion of the bullet in the cluster. We even detect a south to north temperature gradient within the bullet itself. In the Centaurus cluster we detect, by dividing up the luminosity of the cluster in bands of gas temperatures, a striking feature to the north-east of the cluster core. We hypothesize that this feature is caused by a subcluster left over from a substantial merger that slightly displaced the core. We conclude that our method is very powerful in determining the spatial distributions of plasma temperatures and very useful for systematic studies in cluster structure.

Subject headings: galaxies: clusters: individual (Abell 1689, 1E 0657-55, Centaurus) — methods: data analysis — x-rays: galaxies: clusters

1. INTRODUCTION

Early work on X-ray emission from clusters of galaxies, based on X-ray data obtained with instruments of modest angular and spectral resolution, implied that the profiles of X-ray emission are smooth and the spectra can be adequately described as nearly-isothermal hot plasma, generally indicating relaxed structure. This picture has changed markedly with precise imaging data from the Chandra and XMM-Newton instruments: X-ray images of clusters reveal complex intensity distribution, where in general, the surface brightness lacks circular symmetry. The cluster emission cannot be described by a single temperature, or even spherically-symmetric but radially-dependent temperature distribution (e.g. Markevitch et al. 2000). In addition, simple but well-motivated models such as "cooling flows" fail to adequately describe the observations (e.g. Peterson et al. 2001), even for clusters that are otherwise "relaxed." This is likely due to a complex history and physical processes associated with the cluster formation, which is yet to be fully understood. Such complexity may include effects of recent merger activity, large-scale "bubbles," presumably due to the interaction of the outflows produced by the central active galaxy, or sharp abundance gradients associated with recently triggered star formation; or other, still unknown processes (Sanders et al. 2004). Clearly, an analysis technique not relying on symmetry of flux or temperature distribution is needed.

The methods considered for this task include fitting isothermal spectra to fixed or adaptively-binned grids of photons across the detector plane (e.g. Markevitch et al. 2000; Sanders et al. 2004). Another approach is imaging deprojection or "onion-peeling" methods (e.g. Fabian, Cowie & Grindlay 1981), which in turn have been extended to spectroscopic deprojection (Arabadjis, Bautz & Garmire 2002; Arnaud 2001; Kaastra et al. 2003; Andersson & Madejski 2004). An alternative method, developed recently by some of us and termed "smoothed particle inference" or SPI (Peterson, Marshall, & Andersson (2007); hereafter PMA07) relies on a description of a cluster as a large set of "primitives," which in our case are smoothed particles, or "blobs." Each of those is described by overall luminosity and a spatial position, but also by a Gaussian width, a single temperature, and a set of elemental abundances. A large set (well upwards of a hundred) of such primitives is then propagated through the instrument response using Monte Carlo techniques, and their parameters adjusted via the use of Markov chain methods to optimize the likelihood of the distribution as compared against the observation. The resulting distribution is then a good "non-parametric" description of the cluster. Since the likelihood calculation does not have to be limited to a single instrument, but can potentially include multiple X-ray instruments or even data from other kinds of measurements (such as gravitational lensing, Sunyaev-Zeldovich data, or optical velocity dispersions), the method is quite general. This method is also well suited to analyze other complex, spatially resolved objects where the observed X-ray emission might consist of superposed separable components with varying

Work supported in part by US Department of Energy contract DE-AC02-76SF00515

spectral parameters such as in supernova remnants.

In this paper, we describe the implementation of the method to the observations obtained with the XMM-Newton imaging detectors, known collectively as the European Photon Imaging Camera (EPIC). We apply the method to data from three clusters of galaxies, namely Abell 1689, RXJ 0658-55, and the Centaurus cluster. All three clusters exhibit substantial degree of complexity, and furthermore, all three have good quality, deep XMM-Newton observations, which in turn can be compared against previous X-ray analyses as well as data from other instruments such as the Chandra observatory. In particular, Abell 1689 is likely a merger or a superposition of two components aligned close to the line of sight (Andersson & Madejski 2004, e.g.); RXJ 0658-55 reveals an on-going merger close to the plane of the sky (Markevitch et al. 2002); and the Centaurus cluster shows abundance gradients as well as filaments and bubbles, presumably caused by the energy deposited in the cluster by the central radio source (Fabian et al. 2005). The choice of objects should provide a good illustration (or a test) of the method for three quite different cases. To perform this analysis we constructed a Monte Carlo for the XMM-Newton EPIC detectors analogous to the MC some of us developed for the Reflecting Grating Spectrometer (RGS) (Peterson, Jernigan, & Kahn 2004). However, here we use the MC within the implementation of our Markov chain based method, SPI, described above.

In Section 2, we summarize the SPI method; in Section 3, we describe the specifics of the XMM EPIC response function used here, which includes the effects of the XMM-Newton mirror and the PN and MOS detectors. In Section 4, we briefly describe the previous and current observations of the three clusters and summarize the data reduction procedures. In Section 5, we discuss the application of the SPI method to the XMM-Newton data, and this includes our approach to accounting for the background. Finally, in Section 6 we discuss the results of the analysis, and summarize the paper in Section 7.

2. SMOOTHED PARTICLE INFERENCE

The method of Smoothed Particle Inference (SPI), constructed to model diffuse X-ray emitting astrophysical sources, is described in PMA07. Here we only give a brief summary of the basic features of the method.

In order to describe currently observed diffuse X-ray sources a model with thousands of parameters in required. Our choice of model is a set of spatially Gaussian X-ray emitters of an assigned spectral type. Each Gaussian "blob" is described by a spatial position, a Gaussian width and a set of spectral parameters. For X-ray emitting thermal plasmas the spectral model will be described by a temperature, a set of elemental abundances and an overall luminosity. The reason for the choice of luminosity as the basis for our model rather than gas density is that we do not have to assume anything about the underlying density distribution. This way we model only the observable emission and "blobs" of different properties can simply be superimposed on each other to give the model flux. The three-dimensional structure of the source is not modeled but can be constructed later considering various assumptions regarding the extent of the structure in the third dimension but starting from the same the two-dimensional final model. This process would involve assigning the particles with z-coordinates while keeping the overall structure as spherical as possible without changing any of the x or y coordinates of the particles.

In the Monte Carlo simulation, the flux of the astrophysical source at each energy and spatial position is converted to a prediction of the number of photons detected at a given detector position and energy. We calculate the probability of detection D given the instrument response R and the source model flux F;

$$D(x,y,p) = \int dE\ d\theta\ d\phi\ R(x,y,p|\theta,\phi,E)\ \frac{d^2F}{dE\ d\theta\ d\phi}. \quad (1)$$

Here (x,y) is the position on the detector, p is the observed pulseheight, (θ,ϕ) are sky coordinates and E is the photon energy. This integral is calculated by simulating photons sequentially while taking into account mirror and detector characteristics (described in the next section). The response functions are calculated on coarse grids and interpolated using a Monte Carlo method.

The goodness of fit of the model is calculated from the likelihood function of the model parameters. The model data consists of a finite number of simulated photons and we use a two-sample likelihood statistic to assess the goodness of fit. The data and simulated photons are binned on the same three-dimensional adaptive binning grid. Bins are rectangular in the (x,y,p) data space and the size of the bin is set by requiring a minimum number of photons per bin.

We explore the parameter space of the model with the Markov Chain Monte Carlo (MCMC) method. The high dimensionality of the parameter space requires a method capable of exploring this space without being trapped in local minima. MCMC is very efficient in this returning a list of sample models all consistent with data and whose density in parameter space is proportional to the probability density.

In the scheme of modeling astrophysical sources we have found that dealing with the large number of parameters in smoothed particle fits requires a Markov chain step with an adaptive proposal distribution. We use a Gaussian step with a variable width depending on parameter history with some included memory loss.

We also find it necessary to make some parameters coupled. These are the same for all particles and vary simultaneously. This is the case for the equivalent hydrogen column and sometimes the redshift of the plasma. These parameters will be referred to as global parameters. All other parameters are individual for all particles, vary independently and are referred to as local.

Since we simulate the model photons and bin them on the same grid as the data photons before we compare them there will be inherent Poisson noise in the model. To reduce this effect we over-simulate the model using more photons than what is in the data. We have shown in PMA07 that a value of this over simulating factor of 10 or more greatly improves the results.

The choice of the number of particles used in the model depends somewhat on the complexity of the data but usually a higher number is preferred. A Bayesian evidence calculation (see PMA07) shows that a number of 700 greatly increases the results for a cluster of moderate complexity.

3. THE XMM EPIC AND ITS RESPONSE FUNCTION

The ESA XMM-Newton satellite was launched on December 10, 1999 and consists of three co-aligned X-ray telescopes and a 30 cm optical/UV telescope. Each XMM telescope uses a configuration of 58 nested shells of gold-coated mirrors. The X-rays are reflected twice: by paraboloid/hyperboloid mirrors. This configuration provides high effective area and good angular resolution.

In two of the telescopes $\sim 56\%$ of the photons are intercepted by a Reflection Grating Assembly (RGA) and are dispersed onto 9 metal oxide semiconductor (MOS) CCDs for spectroscopy. The RGA and the CCDs form the Reflection Grating Spectrometer (RGS). The remaining photons that are not intercepted are focused onto an array of 7 MOS CCD chips for imaging spectroscopy. The third X-ray telescope focuses directly onto an array of 12 pn semiconductor chips for imaging spectroscopy. The main differences between the pn and MOS semiconductors is that pn has a better ability to detect photons in a wider energy-range than MOS and that the MOS pixels are smaller ($1.1''$ vs $4.1''$). The MOS and pn mirror and detector assemblies constitute the European Photon Imaging Camera (EPIC).

The full details of the EPIC camera are covered in Ehle et al. (2006) and its latest calibration is described in Kirsch (2006). This section briefly describes the EPIC response function as calculated by use of the XMM Current Calibration Files (CCF) library[1] and explains how it is used in the Monte Carlo. A detailed description of the response calculation and interpolation is described in Peterson, Jernigan, & Kahn (2004) for the XMM RGS Monte Carlo. For EPIC the detector response is different in structure, but the Monte Carlo process is the same.

In summary the response probability function of the EPIC cameras can be written as

$$R(x,y,p|\theta,\phi,E) = A(E)\times v(\theta,\phi,E)\times psf(x,y|\theta,\phi,E)\times v_R(E)\times f(E)\times q(E)\times r(p|x,y,E)\times i(x,y) \quad (2)$$

where $A(E)$ is the mirror effective area, $v(\theta,\phi,E)$ is the mirror vignetting, $psf(x,y|\theta,\phi,E)$ is the energy-dependent point spread function (PSF), $v_R(E)$ is the RGA vignetting, $f(E)$ is the filter transmission, $q(E)$ is the quantum efficiency, $r(p|x,y,E)$ is the pulse-height response and $i(x,y)$ is an exposure map correcting for bad pixels and differences in exposure time between different CCDs.

This function gives the probability of detecting a photon of energy E originating at sky coordinates (θ,ϕ) as an event of pulse-height p at detector coordinates (x,y).

The details of these parts of the detector response is given below.

3.1. *The X-ray Telescope (XRT)*

The XRT response is described by the mirror effective area, mirror vignetting, point spread function and the vignetting caused by the intercepting Reflection Grating Assembly (RGA).

3.1.1. *Effective Area and Vignetting*

The effective mirror collection area of the XMM mirrors is a function of energy and decreases with off-axis angle. This decrease is known as vignetting and is caused by shadowing from neighboring mirror shells. We obtain the on-axis effective area $A(E)$ and vignetting $v(\theta,\phi,E)$ for each telescope from the XMM calibration files[2]. The response files are interpolated linearly and rebinned in order to optimize the performance of the Monte Carlo simulation. The binsize for $A(E)$ is set to 50 eV ranging from 0 to 10.45 keV. The $v(\theta,\phi,E)$ bins are 0.75 keV wide in energy and 0.01 degrees wide in off-axis angle.

3.1.2. *Point Spread Function*

We use a circular symmetric approximation for the PSF as it is described in the calibration files. For on-axis extended sources of $< 10'$ in radial extent this is a sufficient approximation for our purposes. Here we approximate the PSF by use of the encircled energy for different photon energies available from the CCF[3] We use encircled energy samplings for photon energies from 0 to 9 keV with a 1.5 keV spacing. For each energy band the encircled energy is sampled at $1.37''$ intervals out to $9'$ from the center of the PSF. The encircled energy at 1.5 keV is shown in Fig. 1.

3.1.3. *RGA Vignetting*

In the MOS cameras a fraction of the photons are intercepted by the RGA with some energy dependence. This loss of photons for MOS1 and MOS2 is tabulated in the calibration files[4]. In our Monte Carlo model we use a sampling of this energy dependence of 0.5 keV.

3.2. *The PN and MOS CCD Cameras*

3.2.1. *Filter Transmission*

The transmission of the optical blocking filters aboard XMM is modeled for the Thin, Medium and Thick filter configurations as a function of energy. We rebin the transmission as found in the existing calibration files[5] into bins of 50 eV. Filter transmission multiplied by mirror effective area for MOS1 with the Thin filter configuration is shown in Figure 2.

3.2.2. *Quantum Efficiency*

The ability of the detector CCDs to detect photons as a function of energy, or quantum efficiency, is tabulated in the CCF response files[6]. We rebin the quantum efficiency for the Full Frame mode for MOS and both Full Frame and Extended Full Frame modes for PN. We bin the QE in the range from 0 to 12 keV with 15 eV spacing.

[1] All calibration data was obtained from ftp://xmm.vilspa.esa.es/pub/ccf/constituents/

[2] XRT1_XAREAEF_0008.CCF XRT2_XAREAEF_0009.CCF and XRT3_XAREAEF_0010.CCF.

[3] XRT1_XENCIREN_0003.CCF, XRT2_XENCIREN_0003.CCF and XRT3_XENCIREN_0003.CCF.

[4] RGS1_QUANTUMEF_0013.CCF and RGS2_QUANTUMEF_0014.CCF in FITS extension RGA_OBSCURATE.

[5] EMOS1_FILTERTRANSX_0012.CCF, EMOS2_FILTERTRANSX_0012.CCF and EPN_FILTERTRANSX_0014.CCF.

[6] EMOS1_QUANTUMEF_0016.CCF, EMOS2_QUANTUMEF_0016.CCF and EPN_QUANTUMEF_0016.CCF.

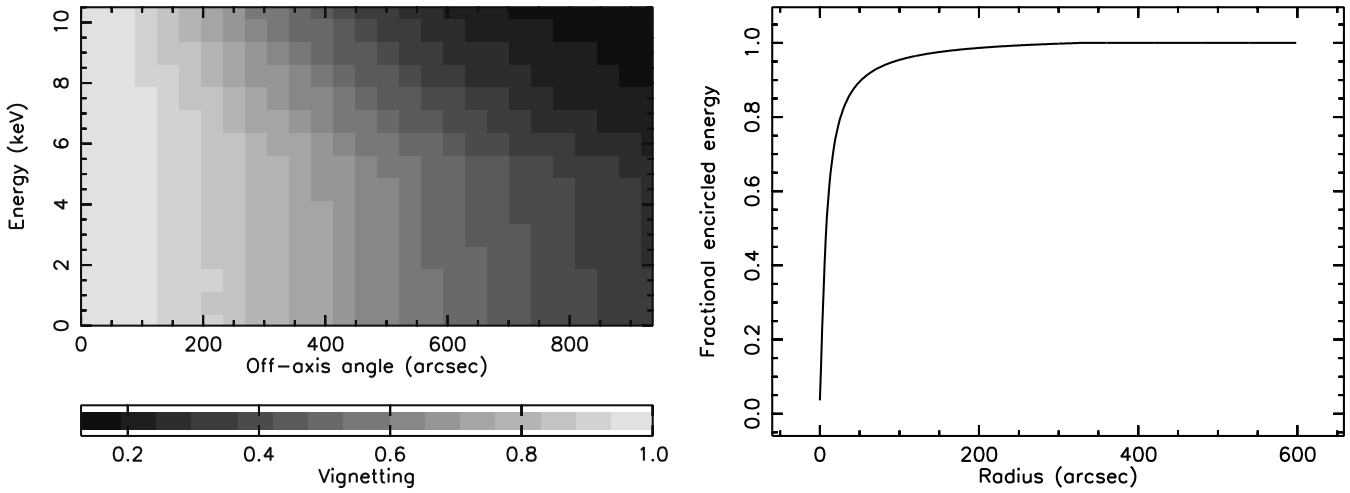

FIG. 1.— The fractional loss of photons due to vignetting as a function of off-axis angle and energy (Left). Encircled energy as a function of radius for the XRT1 on-axis monochromatic PSF at 1.5 keV (Right).

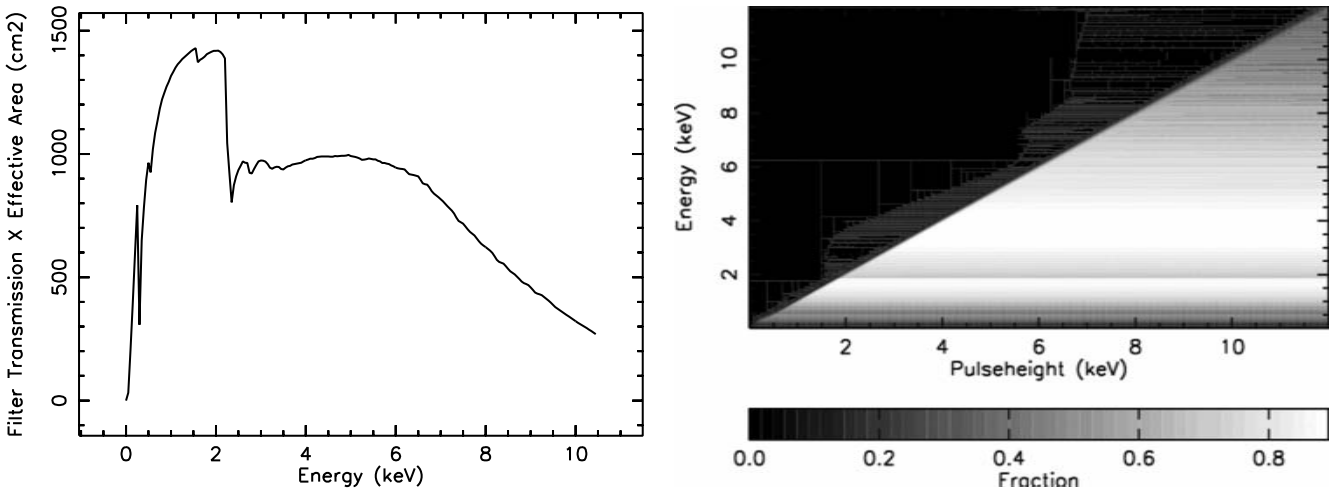

FIG. 2.— Filter Transmission multiplied with effective area for the MOS1 camera in the Thin filter configuration (Left). Quantum efficiency multiplied by the pulseheight re-distribution function for MOS1 is shown as of revolution 534 (Right). The cumulative probability of detecting a photon with a certain pulseheight (x-axis) is shown as a function of incoming energy (y-axis).

3.2.3. *Pulseheight Re-distribution Function*

EPIC pn response matrices are available from the XMM SAS homepage[7]. In the pn detector the CCD response of the 12 CCDs varies with the distance from the line separating the two CCD rows. PN response matrices are available for every 20-pixel rows from rows 0-20 (Y0, at the edge) to rows 181-200 (Y9, at the center). In the Monte Carlo simulation we calculate the distance from the detector center line and use the correct PN response matrix accordingly. We only use matrices for the Full Frame and Extended Full Frame observing modes and only for event pattern 0-4 (singles and doubles) for PN.

EPIC MOS response matrices are dependent on observing epoch and should be chosen according to the satellite revolution when the observation was taken. We use the XMM SAS command `rmfgen` to generate MOS response matrices for 14 different epochs from revolution 101 to 1021. In the Monte Carlo we choose whichever epoch is closest to the observation. For MOS we use imaging mode matrices with all event patterns (0-12, singles, doubles, triples and quadruples). Recently, it has been discovered that the MOS response is also dependent on distance from the detector axis (see XMM-Newton EPIC Response and Background File Page, update 2005-12-15[8]). In the XMM CCFs the response is modeled in three different regions; a "patch", "patch wings" and outside "patch". Therefore we also generate response matrices for all these three regions for each epoch. In the MC all three are read in for the epoch in question and the correct one is chosen based on the location of the detected photon.

The PN response matrices are rebinned to a constant 15 eV binsize 800×800 matrix from 0.05 to 12.05 keV for

[7] ftp://xmm.vilspa.esa.es/pub/ccf/constituents/extras/responses/

[8] http://xmm.vilspa.esa.es/external/xmm_sw_cal/calib/epic_files.shtml

both energy and pulseheight. MOS matrices have 15 eV binsize and run from 0 to 12 keV. These matrices are integrated over pulseheight to form cumulative distributions. A sample response matrix from the MOS1 detector (rev. 534) multiplied with quantum efficiency is shown in Fig. 2.

3.3. *Response Calculation*

In the Monte Carlo, photons are generated via probability density functions normalized to unity. We calculate the cumulative distribution by integrating the probability functions and then draw a number from 0 to 1 at random to choose a particular photon property. First, photons are chosen from a model function with a given set of input model parameters. The output variables are the photon energy and sky coordinates (e, θ, ϕ). Second, we predict the detector coordinates and pulseheight (p, x, y) by drawing photons using response function R. In order to maintain the proper effective area and exposure normalization, photons are sometimes discarded according to the proper response functions (i.e. mirror effective area, filter transmission, vignetting, quantum efficiency and exposure map). The response functions in 2 are in general not analytic and have to be stored in memory on grids. In order to limit the amount of used internal memory we save the functions on coarse grids (see previous subsection) and interpolate linearly to get intermediate values.

4. CHOICE OF TARGETS, OBSERVATION DETAILS, AND DATA REDUCTION

Here, we describe the choice of targets selected to demonstrate the capabilities and versatility of our method. The three chosen targets span a broad range of complexity of the flux, temperature, and redshift. Note that the exact same analysis chain is applied to all objects.

The data were reduced using standard pipeline processing as of XMM `SAS` version 6.5 producing photon event lists. For the screening of soft proton flares we create light-curves in the 10 - 12 keV band for MOS and the 12 - 14 keV band for pn in 100 s bins. We discarded the data when the total flux reached 3σ above the quiescent level (cf. Pratt & Arnaud 2002). After this cut we perform a similar second cut on the soft flux light-curves in the 0.3-10 keV band for MOS and the 0.3-12 keV band for pn binned by 10s. We use all event patterns (singles, doubles, triples, quadruples) for MOS and singles and doubles only, for pn. We also require `XMMEA_EM` for MOS and `XMMEA_EP` for pn and also `FLAG`=0.

Using SAS command `eexpmap`, we create exposure maps with $1'' \times 1''$ bins in detector coordinates for all detectors. These account for bad pixels and columns in the data and correct for varying exposure over the CCDs. An example of an exposure map for the MOS1 detector during the Abell 1689 observation is shown in Figure 3.

4.1. *Abell 1689*

This cluster is one of the best studied objects with gravitational lensing techniques, as the optical images clearly reveal arcs and arclets allowing strong lensing analysis (Tyson & Fischer 1995). Deep studies with the ESO MPG Wide Field Imager provide additional constraints towards the determination of the cluster gravitational potential, via the use of weak lensing (Clowe & Schneider 2001; King et al. 2002). More recently, the mass profile has been detailed further using combined strong and weak lensing using HST/ACS and Subaru images (Broadhurst et al. 2005). The optical data (including studies of galaxy velocities) indicate that the cluster contains sub-structures (Miralda-Escude & Babul 1995; Lokas et al. 2006). The early X-ray data for this cluster indicated an X-ray intensity profile implying a single, relaxed system, but the mass determination from the X-ray analysis indicated a lower mass (by about a factor of 2) than the mass value determined from lensing (Miralda-Escude & Babul 1995, e.g.).

The analysis of the XMM-Newton observation used in this paper, but using more traditional techniques than the SPI method, was presented by Andersson & Madejski (2004), and we refer the reader to that paper for more extensive discussion of Abell 1689's properties as well as previous X-ray observations. In summary, the X-ray emission appears symmetric, and the average temperature inferred for the region of $3'$ in radius is 9.3 ± 0.2 keV, assuming the Galactic column of 1.8×10^{20} cm^{-2} of Dickey & Lockman (1990). However, the spatial analysis indicates that the temperature of the emitting plasma is clearly not uniform, ranging from ~ 7 to ~ 10 keV, with a hint of a temperature gradient in the southwest - northeast direction. In addition, the redshift of the emitting gas as inferred from the X-ray spectrum varies across the image, with a high-redshift structure to the east, with $z = 0.185 \pm 0.006$, separated from the rest of the cluster at $z = 0.17$. This indicates that the cluster consists of two components in projection, which either have started to merge, or are falling towards each other. One of the premises of our study is to determine if the two sub-components are indeed related, or if they should be treated as two separate clusters that happen to be located close to the same line of sight in the sky and observed in projection against each other.

For the SPI analysis below, we use the same data set as reported in Andersson & Madejski (2004). Specifically, the observation was conducted for 40 ks on December 24, 2001, during the revolution 374, but the data were reduced using a more recent version of the SAS software (see above). After screening the raw data according to the criteria below, the net observation time and counting rates were 37 ks / 4.4 ct s^{-1} for the MOS cameras, and 29 ks / 15 ct s^{-1} for the `pn` detector.

4.2. *RXJ 0658-5557*

RXJ 0658-5557 (or 1ES 0657-56) at $z = 0.296$ was first discovered as an extended X-ray source by the Einstein IPC (Tucker, Tananbaum, & Remillard 1995) and was later found from ASCA data (Tucker et al. 1998) to have a temperature of about 17 keV, although subsequent simultaneous analysis of Asca and ROSAT PSPC data by Liang et al. (2000) suggested a lower value, of $14.5^{+2.0}_{-1.5}$ keV. Still, even the revised value of the temperature makes it one of the hottest known clusters. The disturbed profile of the X-ray emission seen in the ROSAT observation suggests an on-going merger (Tucker et al. 1998). Furthermore it is associated with a powerful radio halo (Liang et al. 2001), probably radiating via the synchrotron process, and suggesting the presence of a population of ultra-relativistic particles. RXJ 0658-5557 was

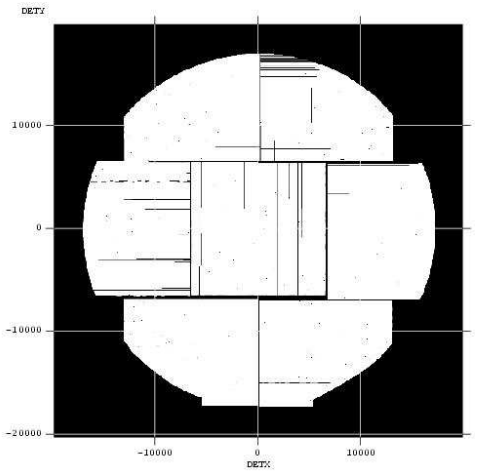

FIG. 3.— MOS1 exposure map from Abell 1689 observation.

first observed by Chandra in October 2000 with 24.3 ks of usable data (Markevitch et al. 2002) and now has a total of over 500 ks of Chandra exposure clearly revealing the bow shock in front of the "bullet" emerging from the merger. The collision is clearly supersonic with a Mach number of 3 deduced from the angle of the Mach cone.

The XMM data for the cluster have been analyzed previously in Zhang et al. (2004) and Finoguenov, Böhringer & Zhang (2005) who find an average temperature of $13.59^{+0.71}_{-0.58}$ keV using data in the 2-12 keV range and fixing the n_H to the Galactic value of 6.5×10^{20} cm^{-2} (Dickey & Lockman 1990). In addition, the XMM-Newton data have been used in joint spectral fits with the RXTE data (in the context of the search for hard X-ray emission) by Petrosian, Madejski, & Luli (2006), where the hard X-ray flux would be by Compton scattering of the Cosmic Microwave Background by the same relativistic particles that are responsible for the radio emission. In their analysis, Petrosian, Madejski, & Luli (2006) use the MOS and pn data in the range of 1.0 - 10.0 keV, and, adopting the absorbing column to be that measured for our Galaxy of 4.6×10^{20} cm^{-2} by Liang et al. (2001), they infer an average temperature for the region within $4'$ radius to be 12.0 ± 0.5 keV, in a marginal agreement with that determined by Finoguenov, Böhringer & Zhang (2005), with the difference probably due to the use of different bandpass, calibration files, and the assumed absorbing column density.

In similarity to Abell 1689, the spatial structure of the gravitational potential in this cluster has been extensively studied using both strong and weak gravitational lensing. Weak lensing analysis by Clowe, Gonzalez & Markevitch (2004) and more recently, joint weak and strong lensing analysis by Clowe et al. (2006) and Bradac et al. (2006) reveal a striking offset between the peaks in the gravitating material and x-ray luminous matter. This suggests a scenario where the subclusters have collided head-on, and the gas is being slowed down by ram pressure, while the dark matter is able to pass through more or less without resistance. As such, this cluster offers one of the most compelling arguments for dark matter – interacting only via gravitation – being distinct from the baryonic material, responsible for the X-ray luminosity.

For the SPI analysis, we extracted and analyzed data collected during the XMM-Newton pointing on 2000 October 20 - 21; this is the same XMM-Newton observation as reported in Zhang et al. (2004); Finoguenov, Böhringer & Zhang (2005), Petrosian, Madejski, & Luli (2006) (see above). After cleaning, the effective exposure times and total gross (not background-subtracted) counting rates are 25 ks / 3.3 ct s^{-1} for the MOS1 data, 25 ks / 3.3 ct s^{-1} for the MOS2 data, and 22 ks / 9.9 ct s^{-1} for the pn data.

4.3. *Centaurus cluster*

The Centaurus cluster, also known as Abell 3526, is one of the most nearby clusters, and with this, it allows good spatially-resolved studies of cluster structure. It is a relatively cool cluster, at an average temperature of $kT = 3.68 \pm 0.06$ keV (Fukazawa et al. 1998), with a modest luminosity. One of its distinguishing characteristics is the detection of spatially-resolved gradients of elemental abundances, even with data of modest angular resolution (see, e.g., Fukazawa et al. 1994; 1998). This, as well as a wide distribution of temperatures of the emitting plasma, are clear in the Chandra data (Fabian et al. 2005), where the X-ray image shows a "swirl" in the central structure with a filament extending towards the northeast. In Sanders & Fabian (2006) the XMM data is analyzed in combination with the Chandra data in order to derive maps of abundances for separate elements.

In the SPI analysis, we used the data set collected on January 3, 2002. After cleaning, the effective exposure times and total gross (not background-subtracted) counting rates are 46 ks / 18 ct s^{-1} for the MOS1 data, 46 ks / 18 ct s^{-1} for the MOS2 data, and 42 ks / 60 ct s^{-1} for the pn data.

5. APPLYING SPI TO THE DATA

5.1. *Data Binning*

In the framework of SPI, a three dimensional adaptive binning technique is used to bin the photon event lists. The details of this are described in PMA07. The bins are

rectangular in shape and are chosen so that each bin with 20 photons or more is split in two. The binning allows for different weighing of the dimensions (x, y, pulseheight) so that one dimension may be binned more finely than another. We choose to make the bin sizes in pulseheight on average 10 times smaller than the x and y bins. For RXJ 0658-55 this results in 14361 bins with 13.3 photons per bin on average and for the A1689 data we get 31096 bins which equals 13.5 photons per bin on average. For the Centaurus data the binning resulted in 197092 bins with 13.7 photons per bin on average.

For analysis we use MOS data in the 0.3 - 10.0 keV range and PN data in the 1.1 - 10.0 keV range. PN low energy data are cut off due to PN-MOS disagreement at low energies (cf. Andersson & Madejski 2004). In both analyses we restrict ourselves to a $20' \times 20'$ spatial region centered on the respective cluster centers.

5.2. *Spatially Resolved Spectral Model*

To model the cluster emission we use a multi-component model consisting of spatially Gaussian smoothed particles, or "blobs" of cluster emission. Each of these is described by a spatial position, a Gaussian width, a single temperature, a set of elemental abundances and an overall flux. Since each particle in described by a Gaussian there will always be overlapping components. This means that the model everywhere describes a multi temperature plasma.

In this case we set the spectral emission model to be described by the MEKAL (Mewe, Gronenschild, & van den Oord 1985; Mewe, Lemen, & van den Oord 1986; Kaastra 1992; Liedahl, Osterheld, & Goldstein 1995) thermal plasma model with Solar abundances absorbed by a WABS (Morrison & McCammon 1983) absorption model. The prior ranges for all parameters are set to be flat for a fixed range except for the spatial Gaussian sigma which has a logarithmic prior distribution. The midpoint of the spectral parameter ranges is determined from simple spectral analysis using the full cluster emission. The width of the range is chosen from what values are expected for that parameter in the cluster. It is, in general, an advantage to choose a parameter range that is wider than what is expected. We choose to let both the equivalent hydrogen column and the redshift of the cluster plasma be variable in the analyses as well as temperature and metallicity with respect to Solar.

For Abell 1689 the allowed range of n_H is 0 - 3.5 $\times 10^{20}$cm^2, this value is tied to be the same for all blobs. The plasma temperature is variable in the 5 - 11 keV range, metal abundances in the 0.15 - 0.35 Solar range and z from 0.15 to 0.21. The blobs are allowed to move freely over the full $20' \times 20'$ region and have a variable Gaussian sigma ranging from $e^{0.5}$ to $e^{5.5}$ arcseconds.

In the case of RXJ 0658-5557 the situation is similar with allowed ranges for n_H of 2.7 - 3.7 $\times 10^{20}$cm^2, temperature of 1 - 19 keV, metal abundance of 0.12 to 0.32 Solar and z of 0.28 to 0.30. The blobs are again allowed to move freely over the full $20'' \times 20''$ region and have a variable Gaussian sigma ranging from $e^{0.25}$ to $e^{4.25}$ arcseconds. The equivalent hydrogen column is set to be a global parameter, which means that it is the same for all blobs.

For Centaurus the allowed range of n_H is 0 - 2.2 $\times 10^{20}$cm^2. The allowed range of temperatures is 0.5 - 9.5 keV, of metal abundances is 0.1 - 1.5 Solar and z is variable in the range 0 - 0.015. Smooth particle sizes and movement range is the same as for RXJ 0658-55.

In order to describe both the spatial and spectral properties of the clusters adequately we choose to use 700 particles for the A1689 analysis and 600 for RXJ 0658-55 and Centaurus. A justification for this number of particles for datasets of similar complexity can be found in PMA07. However, we also do an analysis using only 100 components in order to check the consistency of the broad spatially varying spectral properties of the clusters.

5.3. *Background Model*

The XMM instrumental background consists of three different main parts; particle background (soft protons), cosmic ray induced internal line emission and electronic noise. In our background model `epicback` the particle background is approximated by a power law spectrum with variable spectral index and a separate normalization for each detector. This part of the model is not propagated through the mirror model but is exposed directly onto the CCDs. In fact, this background component is scattered somewhat by the mirrors and does have a radial dependence (Read et al. 2005). It decreases to about 80 % of its central value $10'$ from the pointing axis. We are working to include this effect. However, here, since we are dealing with bright clusters, we assume that a spatially flat modeling of this background is sufficient.

We determine the best fit parameters of our background model using several EPIC observations with the filter wheel in the closed position[9] and "blank fields" with removed point sources[10] as well as background files compiled by the XMM SOC (Lumb 2002). We find the best fit value of the power-law index to be ~ -0.22 (varying from -0.20 to -0.24 in the different observations) and we choose to fix it at this value in the remaining analysis.

The internal line emission constitutes of fluorescent lines excited by high energy particles in various materials of the detector. These lines include the Al-K, Si-K, Au-M, Cr-K, Mn-K, Fe-K, Ni-K, Cu-Kα, Cu-Kβ, Zn-K, Au-Lα and Au-Lβ complexes. The lines are approximated with delta functions at the respective energies and this is a good approximation considering the limited energy resolution of the CCDs. The emission is assumed to be uniform across the detectors except for the Cu-K emission which is highly non-uniform with a hole, devoid of emission, in the center of the detector plane. We approximate this hole with the intersection of a circle with a $390''$ radius and rectangle $630''$ wide. The relative normalization of these lines is determined individually for MOS and PN detectors using the filter wheel closed observations.

The electronic noise background includes bright pixels and columns, readout noise etc and is modeled as an exponential $F \propto e^{-(E/E_i)}$ with a variable value of E_i, where E is the energy assigned to the noise event. We find an ap-

[9] Observation IDs: 0073740101,0134521601,0134522401,0134720401, 0136540501,0136750301,0150390101,0150390301,0154150101, 0160362501,0160362601,0160362801,0160362901 and 0165160501

[10] Observation IDs: 0147511601,0037982001

propriate value for E_i to be ~ 150 eV when using the MOS cutoff at 0.3 keV and PN cutoff at 1.1 keV. This value is a fixed parameter in the analysis. This noise background is assumed to be spatially uniform.

The fraction of photons going to each of these model components (particle, lines and noise) is variable in the analysis and all have a flat prior from 0 to 1. Also the fraction of photons for each model component going to each detector (MOS1, MOS2, PN) is variable. The total normalization of the background model with respect to the cluster model as well as the hard and soft CXB components is then set as a variable parameter also with a flat prior from 0 to 1.

We model the soft galactic X-ray background using a uniform emission component consisting of a MEKAL spectral model with WABS absorption. The plasma temperature is fixed at 0.16 keV with a metal abundance of $0.3Z_{\odot}$ at $z = 0$ and the absorption is fixed at $n_H = 1.5 \times 10^{20}$ cm^{-2}. Similarly the Cosmic X-ray Background (CXB) - presumably due to superposition of unresolved AGN - is modeled using a powerlaw with $\Gamma = 1.47$ and absorption fixed at $n_H = 1.2 \times 10^{21}$ cm^{-2}. In general, it is customary to use zero absorption for the soft CXB and Galactic absorption for the hard component in CXB analysis (e.g. Hickox & Markevitch 2006). We choose here to use the above values simply due to the fact that it gives a better fit to the data in our analysis of the blank fields mentioned above as well as source free regions outside the clusters analyzed here.

An example of the background model spectrum for two observations with the filter wheel in the closed position is shown in Fig. 4. All parameters of the background models are global.

5.4. *Markov Chain Model Sample*

In the Monte Carlo, photons are simulated according to the probability functions given by the model parameters as described in section 2. The simulated photons are propagated through the detector model and binned on the grid determined by the three dimensional photon density of the data. The two-sample likelihood Poisson statistic is calculated to provide a goodness of fit. In our analysis we use a model-to-data over-simulate factor of 10 for all datasets to reduce the model noise (see Section 2). In principle it would be ideal to utilize a factor as large as possible but we are limited by finite CPU speed and internal memory. In PMA07 we compare different values of this factor and show that the results improve significantly when using a value of 10 or greater. Parameters are iterated by Markov chain sampling as described in the previous Sections.

Figure 5 shows the evolution of the Poisson χ^2 per degree of freedom minus one. Illustrated are (from left to right) values for the 700 blob run for A1689, the 600 blob run for RXJ 0658-55 and the 600 blob run for Centaurus. The statistic approaches a value very close to 1 and stabilizes after ~ 2000 iterations. Below, in the same figure we show the evolution of the Poisson χ^2 per d.o.f. minus one for the control runs with 100 smoothed particles. In general, the runs with more blobs reach a good fit faster and approach a lower value of the fit statistic. Based on these plots we consider the chain to be stable after 2000 iterations when the statistic becomes stationary and close to 1. We only use samples from iteration 2000 to deduce cluster properties in the following sections.

6. FINAL MODEL

To visualize the output model sample we use the methods described in PMA07. We stop the Markov chains after 4000 iterations and assume convergence after 2000 iterations as described above. We are left with 2000 models, each consistent with the data. Each iteration takes approximately 30 minutes on a single Intel Pentium 4 2.0 GHz cpu which results in about 3 months per cluster. The models are filtered and marginalized in order to deduce the cluster properties as discussed below.

6.1. *Abell 1689*

To confirm that we have an overall good spectral fit we plot the model spectrum as inferred from the model sample versus the data and the ratio of the two in Figure 6. This is also seen by looking at the statistic in Figure 5. The plot indicates that we achieved an accurate fit.

To infer the luminosity distribution of the cluster we generate the luminosity map for each model in the sample and take the median in each spatial pixel in order to make the median luminosity map shown in Figure 7 (top right). The map of raw counts from the screened data file is shown on the left for comparison. There is good agreement between the reconstruction and the raw data; specifically, the reconstructed profile is sharper than the data due to PSF deconvolution and the fact that obvious chip gaps in the data are compensated by taking the exposure into account.

We have selected three interesting regions (numbered in Figure 7), motivated by our analysis in Andersson & Madejski (2004) to study in more detail the distribution of plasma temperatures in those regions. First, for a cluster which has quite regular surface brightness distribution – similar to clusters with well-established "cooling cores" – the temperature of the core for Abell 1689 is quite high, ~ 7.5 keV. Second, we have identified a region of hotter plasma, ~ 9 keV, to the north of the cluster core indicating possible shock heating of the gas in that region. Third, we have chosen to study in detail a region south of the core exhibiting a temperature almost as low as the core itself.

Next, we form a median temperature map by first weighing the temperature of each model particle by its luminosity creating a temperature map for each model in the 2000 model MCMC sample. This sample of maps is then averaged by taking the median of the distribution of temperatures for each spatial pixel as is done in the creation of luminosity maps. Instead of taking the luminosity weighted average, in another attempt to visualize the distribution of temperatures in the cluster, we bin the luminosity in bins of temperature in each spatial pixel creating a three dimensional differential luminosity data cube. We do this for all sample models and for each of them calculate the mode of the resulting distribution of each spatial pixel. Taking the median over all model samples of this mode accurately describes the dominant temperature at any given spatial position. We note that this will not give the same value of temperature as one would get from traditional spectral analysis. The temperature measurement is biased due to

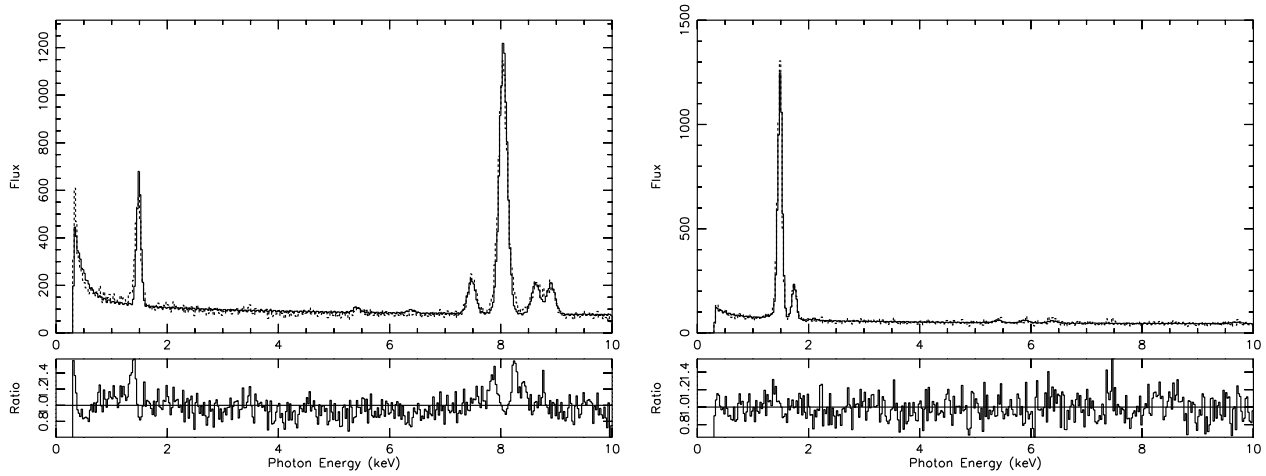

FIG. 4.— Typical background model including electronic noise, internal line emission, particle background from a filter wheel closed observation in PN (Left) and MOS (right). The flux is shown as counts per 25 eV with the data shown as dashed lines and the model as solid. The ratio of the two is shown below.

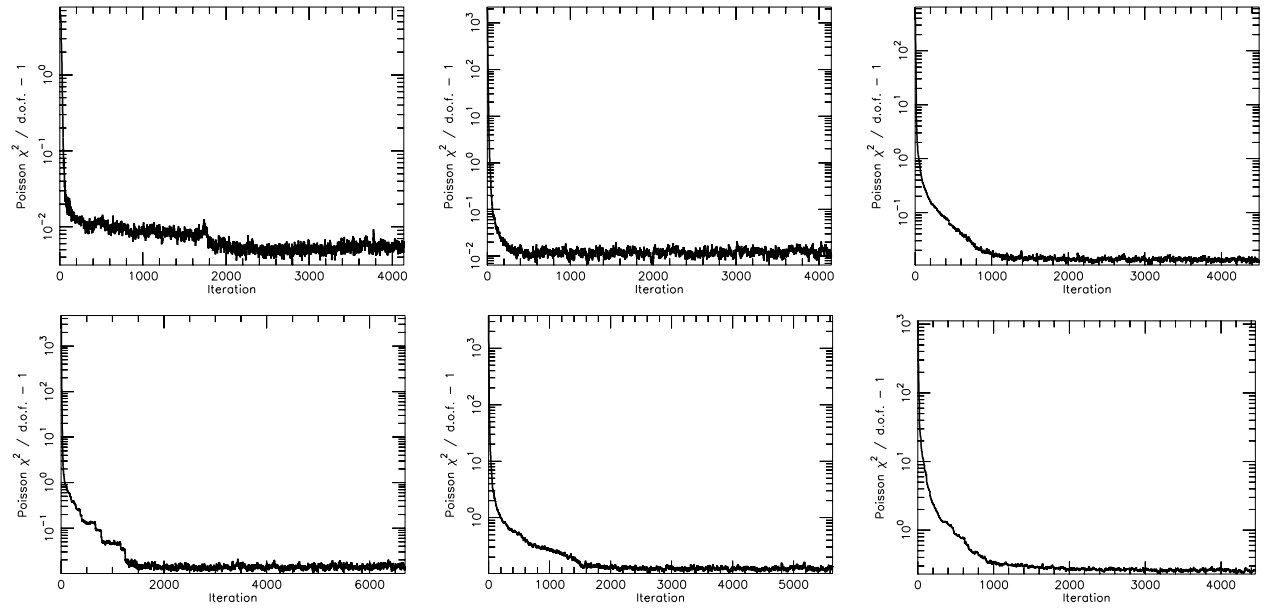

FIG. 5.— Poisson χ^2 per degree of freedom for, top plots: (from left to right), the Abell 1689, RXJ 0658-5557 and Centaurus standard runs (700,600 and 600 blobs respectively), bottom plots: the Abell 1689, RXJ 0658-5557 and Centaurus 100 blob runs .

the degeneracies present in spectral fitting when allowing for 700 separate temperature phases. However, we believe that it is the method of highest contrast when separating distinct temperature components of a galaxy cluster. The median distribution mode and the median emission weighted temperature are shown in Figure 7 (bottom left and right). To display an estimate of the error on the emission weighted temperature we calculate the 1 σ variation on this value over the model sample shown in Figure 8. This value is below 0.5 keV throughout most of the shown region. For all of the calculations above we have used the model run with 700 particles.

In order to study the regions selected above in more detail, we have extracted the differential luminosity distribution in these regions and binned them into 20 bins over the 5 to 11 keV allowed range. We have chosen to use the model run with 100 particles for this in order not to over-complicate the problem. While in this case the luminosity and temperature maps do not show the same level of detail, the distributions of spectral parameters become narrower.

The differential luminosity along with the median of the distribution is shown for these regions in Figure 9. From these data alone we cannot detect any deviation from isothermality in these regions, mostly due to the inherent degeneracies associated with the attempt to fit high temperature emission with a multi-phase model. Since most of the emission is from the bremsstrahlung continuum there are many combinations of gas phases (temperatures) that provide equally good fit to data.

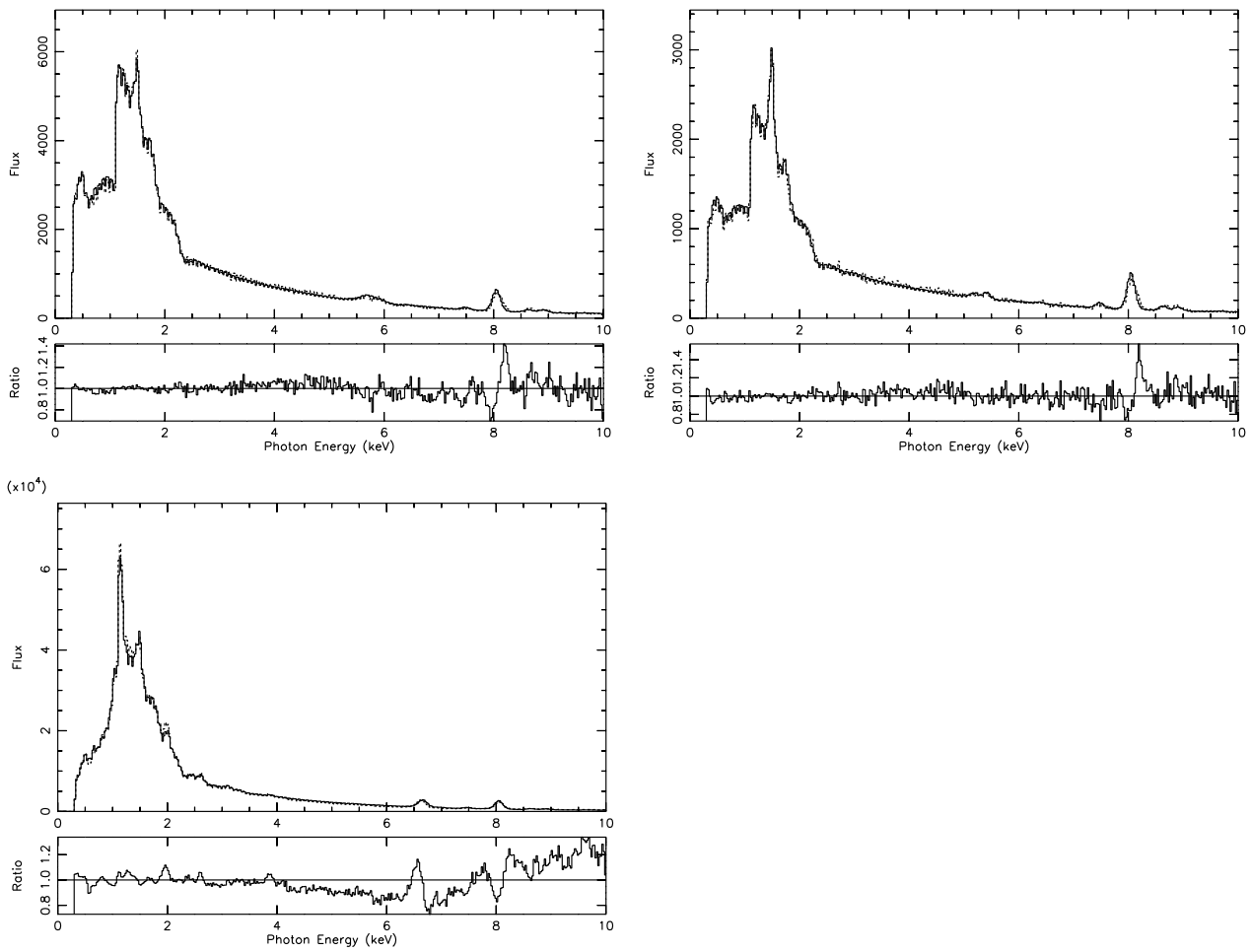

FIG. 6.— Spectral comparison of data (dashed line) to model (solid line) for the Abell 1689 700 blob analysis (Left), the RXJ 0658-55 600 blob analysis (Right) and the Centaurus 600 blob analysis (Bottom) for the full $20' \times 20'$ field used in the analysis. Flux is in units of photon counts per 25 eV bin with the ratio of data to model shown on the bottom. The model spectra are produced by averaging the spectrum from every 100th iteration from 2000 to 4000 and are renormalized to match the data counts.

We have confirmed the existence of a region of hot plasma north of the cluster core as we reported in Andersson & Madejski (2004). This hotter plasma appears to extend approximately in an arc half way around the northern part. The technique verifies both the presence of the colder emission to the south, and the lower than the ambient (by ~ 1 keV) temperature of the cluster core. Our analysis reveals an apparent trail to the south, possibly a remnant tracing the path of the cluster core, and the shock-heated region to the north. However, this could also be due to projection effects from filaments extending in the line of sight direction.

In our earlier findings we infer intra-cluster gas motions from a shift in the position of the Fe-K line complex corresponding to $\Delta z \approx 0.01$. Here we show a map of cluster redshift (Figure 10, Left) similar to the temperature maps shown above. The map was created by calculating the dominant redshift mode at each spatial pixel and taking the median over the samples. The overlayed contours are iso-photon-count from the raw data and the grid is shown for comparison with the regions used in Andersson & Madejski (2004). The results from Andersson & Madejski (2004) is shown in Figure 10 (Right). The map clearly confirms the $\Delta z \approx 0.01$ east-west gradient found previously by us. Here, we can now also assess the significance of this, by analyzing the redshift-mode variation in the model sample. The 1σ model variance of the redshift mode in the regions of interest ranges from 0.016 in to 0.019 and therefore our result has only modest significance, $\sim 1\sigma$. However, we note that it is not clear that the above is the most appropriate estimate of the true uncertainty, since inherent properties of the method could increase the variance: possibly, another means of error estimation could give a more accurate result.

6.2. *RXJ 0658-55*

In similarity to the case of Abell 1689, we plot the model spectrum as inferred from a subsample of the model sample versus the data and the ratio of the two in Figure 6. The plot shows an accurate fit. The evolution of the Poisson χ^2 as a function of Markov chain iteration is shown in Figure 5. As described previously, we generate a median luminosity map from the model and compare with

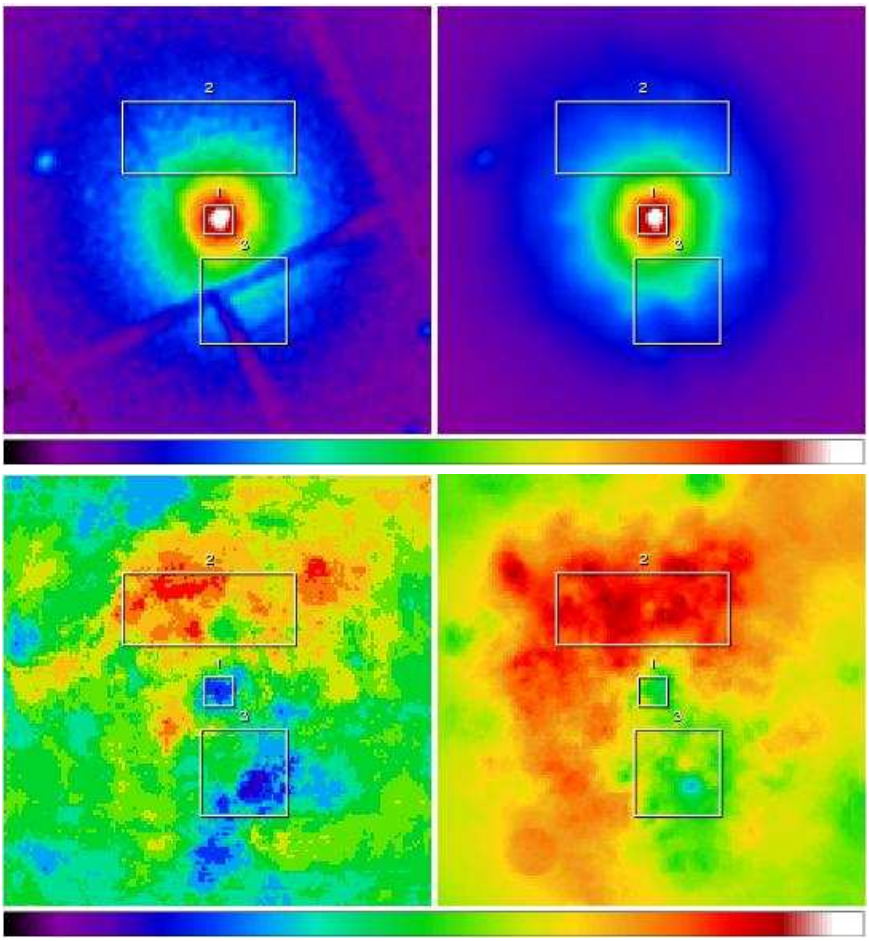

FIG. 7.— Results of analysis for Abell 1689. From left to right; 1. Raw data smoothed by 4″ kernel Gaussian, 2. Luminosity reconstruction using the median of all samples at each spatial point, 3. Temperature map (7 - 9 keV) constructed using the mode of the distribution for all samples at each spatial point, 4. Temperature map (7.5 - 8.5 keV) constructed using the median of the distribution for all samples at each spatial point. All maps show a $5' \times 5'$ region centered on the peak of emission.

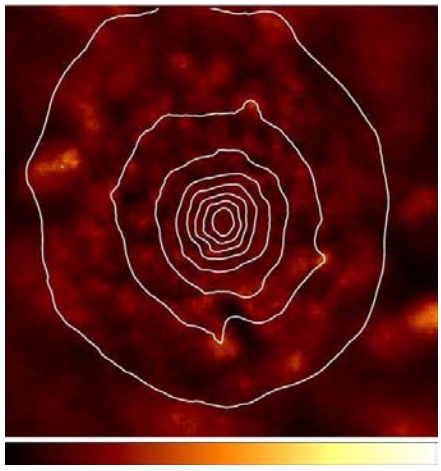

FIG. 8.— Temperature map of A1689 showing the 1 σ variation of the emission weighted temperature in the model sample. The region showed is the same as in Figure 7. Scale limits are from 0 to 1.5 keV.

a counts map smoothed by a 4″ Gaussian (Figure 11 top right and left). It can be seen that the bullet and main cluster features become somewhat sharper by the PSF deconvolution effect from the forward fitting that is inherent in the method.

We form and plot the luminosity weighted temperature map as well as a map based on the dominant temperature mode in Figure 11 (bottom right and left). Both maps

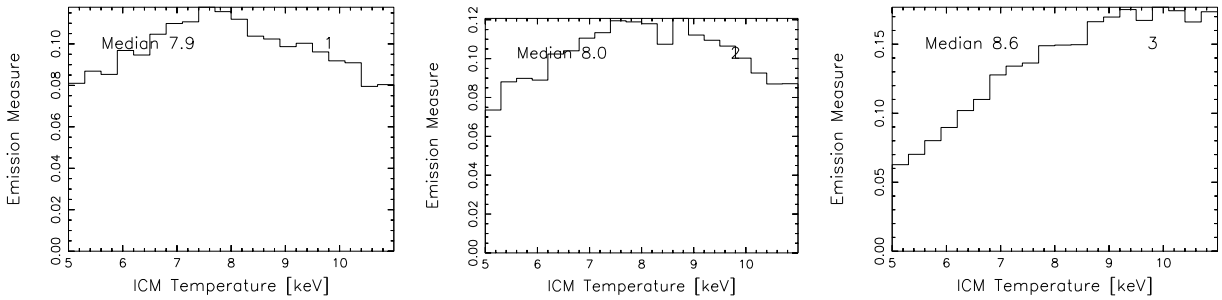

FIG. 9.— Iteration averaged distribution of temperatures for A1689 regions 1 (core), 2 (south) and 3 (north).

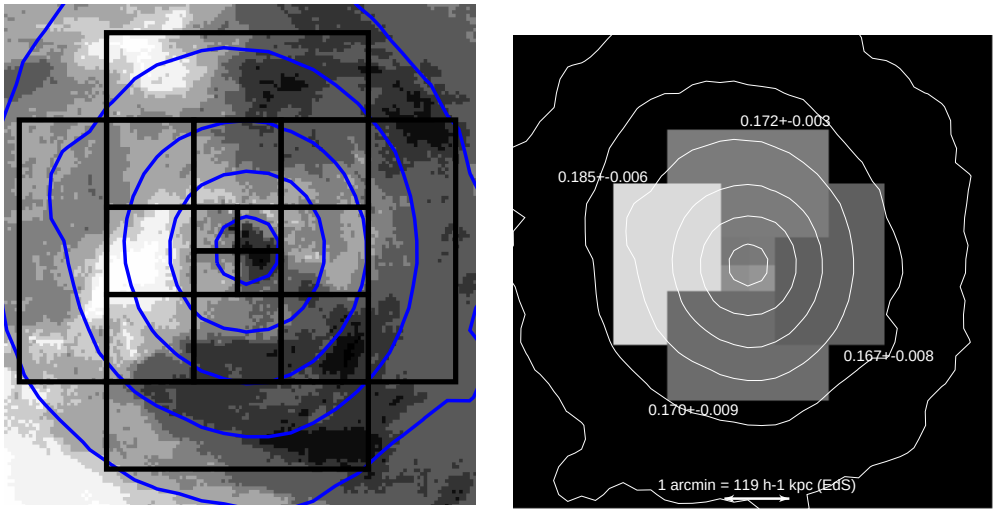

FIG. 10.— Left; Redshift map of Abell 1689 obtained by taking the median of the dominant redshift mode over the model sample. Black to white corresponds to $z = 0.175 - 0.185$. Overlayed contours from the raw event list data and grid regions are from Andersson & Madejski (2004) for comparison. Right; Results from the analysis in Andersson & Madejski (2004)

clearly show the cold core remnant of the "bullet" and the hot shocked gas in front of it. Note that the mode and weighted temperature maps display different properties of the temperature structure and are not comparable. This of course is due to the way we model the plasma in our method. Instead of using just a single temperature as is customary in every spatial region, we use a number of phases that over the model sample form a nearly-continuous distribution. We discuss this further in the paragraph discussing isothermal simulations below. The mode is often biased towards lower temperatures for plasmas with temperatures of 9 keV and lower due to the fact that within the bandpass of epic, at higher T the spectra are more similar to each other and more difficult to distinguish.

We do not see a clear decrease in temperature in front of the shock as expected since the gas should be undisturbed here. It is possible that emission from the post-shock gas is smeared by the XMM PSF and completely dominates the pre-shock emission which in turn would be very faint in comparison. The cold gas of the bullet shows an apparent tail stretching south-east from the bullet center. By looking at the temperature map alone one would conclude that this tail might reveal the movement history of the bullet in the merger. However the luminosity map and, much more clearly, the 500 ks Chandra exposure (Markevitch et al. in preparation), show a symmetrical Mach cone directed westward indicating that this is the direction of motion. The weak lensing analysis (Bradac et al. 2006) also shows the western dark matter halo just west of the bullet. It still cannot be ruled out that the bullet core entered to the north-east of the main cluster (see "entry hole" devoid of emission in this region) proceeding south-west through the main cluster and eventually turning north-west due to the gravitational pull of the dark matter halo located due west thus creating the tail visible in the temperature maps. The dark matter - dominated regions and the gas dominated ones, of course, do not need to have similar merger paths. This scenario is also supported by the apparently previously shock-heated region of gas located directly south of the cluster. This part seems to have almost as hot gas as the shock in front of the bullet. We select this region (no. 6) along with the 6 other regions shown in Figure 11 to do a more detailed analysis.

In Figure 12 we show the detailed distributions of temperatures, in numerical order, from the selected regions above. In region 1 we have extracted the central emission from the cluster core. The distribution clearly shows the signatures of a $kT = 7$ keV plasma with possible contamination from higher temperatures (seen as peaks around 11

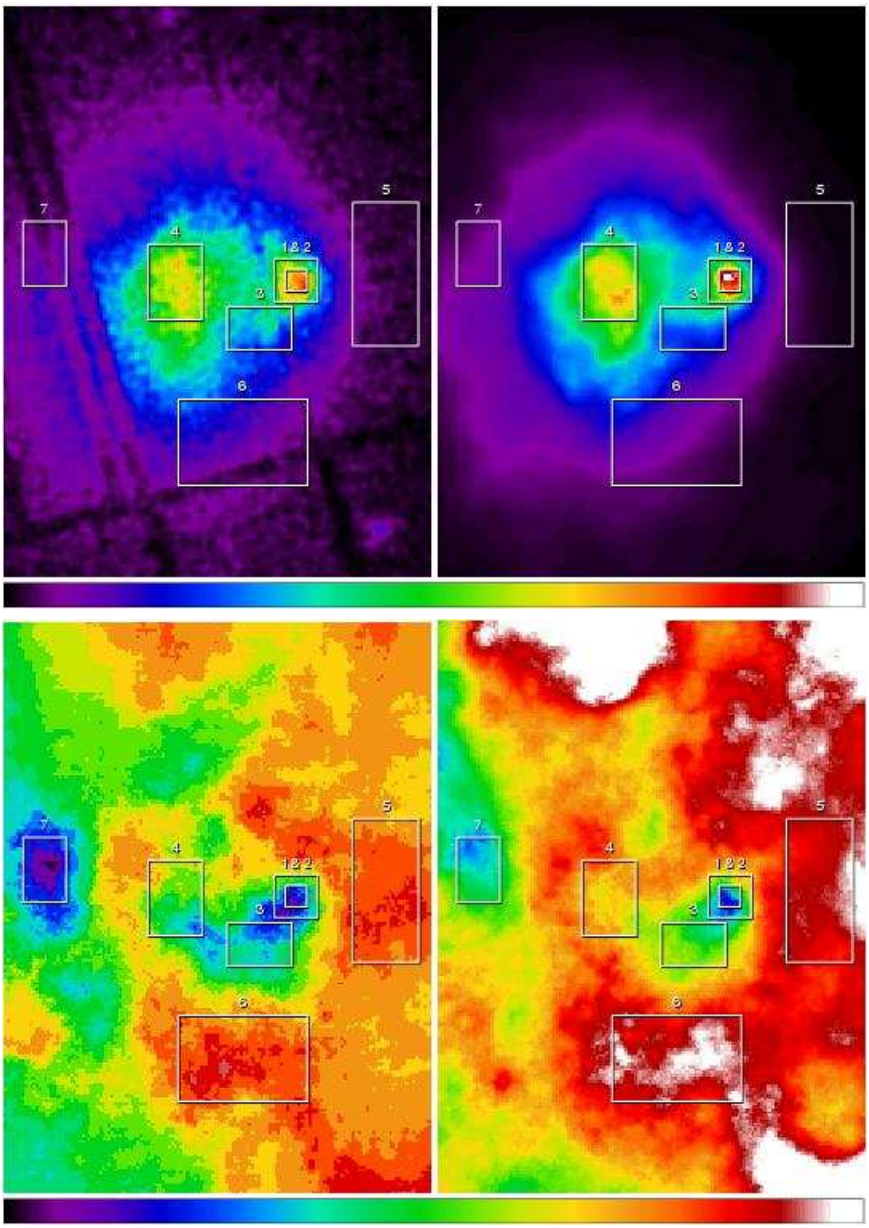

FIG. 11.— Results of analysis for the Bullet cluster. From left to right; 1. Raw data smoothed by 4″ kernel Gaussian, 2. Luminosity reconstruction using the median of all samples at each spatial point, 3. Temperature map (6-13 keV) constructed using the mode of the distribution for all samples at each spatial point, 4. Temperature map (9-13 keV) constructed using the median of the distribution for all samples at each spatial point.

and 14 keV), most likely from projection effects. Regions 2 through 7 show the distributions of various regions in the cluster. In order to determine the deviation from isothermality of the plasma in the selected regions we generated isothermal models of RXJ0658-55 with the same number of photons and the same spatial structure. The isothermal models were reconstructed using the exact same method as the reconstruction of the real data. The distribution of temperatures from the isothermal reconstructions are shown for 4, 7, 10 and 15 keV plasma in Figure 13. None of the distributions in Figure 12 can conclusively be distinguished from an isothermal plasma. However, in the region just in front of the shock (region 5) we see a significant increase around 19 keV which is the highest allowed temperature in our runs. This suggests the presence of very hot gas as expected by shock heating. Limited spatial resolution (as well as the EPIC bandpass) prevent us from a definite determination of this temperature.

Finally we have created luminosity maps of RXJ 0658-55 using emission components in separate bands of temperature. Figure 14 shows the cluster luminosity in the $kT = 1 - 7$ keV, $kT = 7 - 13$ keV and $kT = 13 - 19$ keV bands. The contours are iso-luminosity contours from the $kT = 1 - 7$ keV map. These maps shows an interesting property hinted at by the temperature maps; the bullet appears to move further north with higher temperature. It is possible that this feature indicates an increased compression to the north-west resulting in a higher temperature.

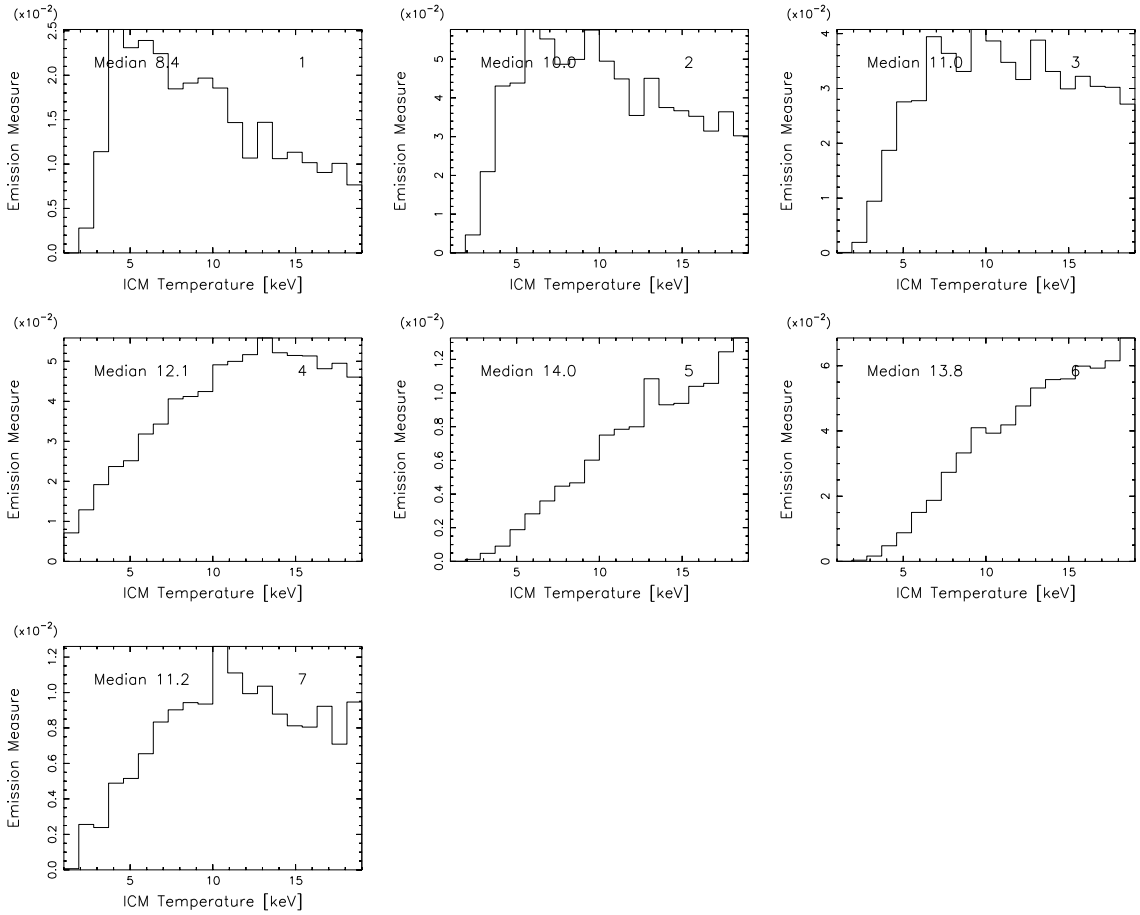

FIG. 12.— Iteration averaged distribution of temperatures for RXJ 0658-55 in regions 1 through 7 also showing the median.

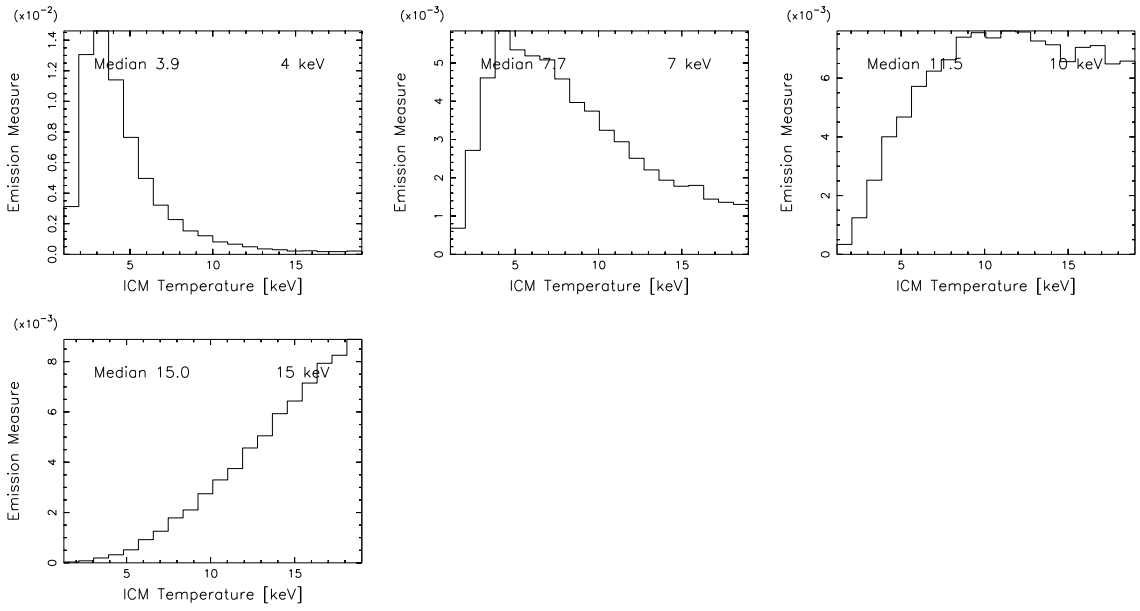

FIG. 13.— Iteration averaged distribution of temperatures for the reconstruction of isothermal simulations of RXJ 0658-5557 due to a 4, 7, 10 and 15 keV plasma.

This is supported by the Chandra image which shows a shorter distance between the bullet and shock front to the north-west than to the south-west.

The three-phase map also clearly shows the extension

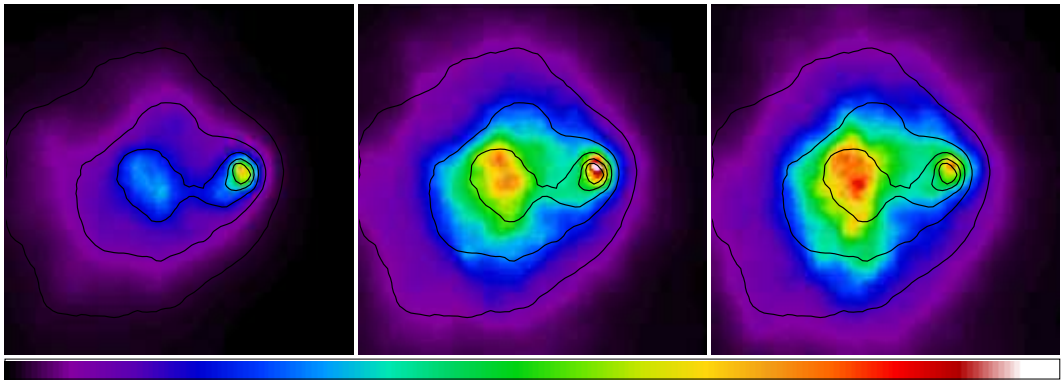

FIG. 14.— Luminosity maps of RXJ 0658-55 in three different temperature bands. From left to right, the ranges are 1 - 7 keV, 7 - 13 keV and 13 - 19 keV.

of hotter gas to the south causing the high temperature region in the temperature maps (region 6).

6.3. *The Centaurus Cluster*

The model spectrum as inferred from the model sample is shown with the data spectrum and the ratio of the two in Figure 6. The model spectrum can be seen to fit the data well and this is confirmed by the Poisson χ^2 in Figure 5.

We form both luminosity and temperature maps analogous to previous sections. In Figure 15 the raw count map of the XMM data (top left) is shown as well as the luminosity reconstruction (top right). Even though the gaps from dead pixel rows are taken into account via the exposure map, some artifacts can be seen. The model aligns itself with the chip gap where a filament extends north-east of the cluster core. Figure 15 also shows a temperature mode map (bottom left) as well as a median temperature map (bottom right). The dominant temperature mode can be seen to be elevated with respect to the median in a hot region north-east in the direction of the filament.

To investigate the temperature in some of the more interesting regions in detail, we created the temperature distributions in four regions and compared them. These plots are shown in Figure 16. The order corresponds to the numbers in Figure 15. Selected regions correspond to the cluster core (1), the extended filament (2), the ambient temperature directly to the west of the core (3) and the anomalously hot region to the north-east (4). The core shows signs of non-isothermality; the distribution includes a narrow peak at 0.5 keV as well as a bump around 1.5 keV, very probably due to projection. In the other plots it is harder to distinguish the distributions from isothermal. However in region 4 there is a hint of a hotter $\sim$ 8keV phase.

For the Centaurus cluster we have focused on a new approach in analyzing cluster structure. In Figure 17 we have produced median maps for the luminosity in bands of different temperatures. From left to right, the Figure shows cluster luminosity in 0 - 1 keV, 1 - 2 keV, 2 - 4 keV, 4 - 6 keV, 6 - 8 keV and 8 - 10 keV temperature bands. This subdivision reveals some striking features; the cluster core is dominant in the 0-1 keV band and apparently it has moved in from north-east, leaving a tail of colder gas. The 1 - 2 keV temperature band map shows a bi-polar nature of this emission around the core. With higher temperatures, the emission becomes more and more offset and in the 8 - 10 keV map shows a concentration of superheated gas in an isolated region to the north-east. Interestingly, this feature is aligned with a filament extending from the cluster core. Possibly, these two irregular phenomena are related.

Finally, we explore the metallicity structure of Centaurus by creating a median metal abundance map analogous to the creation of median temperature maps. The metallicity map is shown in Figure 18 and confirms previous findings by Fabian et al. (2005) and Sanders & Fabian (2006) that the metallicity increases by about a factor 2 (from 0.5 to 1.0 Solar) towards the center. However in contrary to Fabian et al. (2005) we do not find metal abundance levels as high as twice the Solar value and we also do not see a sharp decrease towards 0 in the very center. A minor dip can however be distinguished. It is most likely that both the absence of very high metallicity and the sharp central feature are due to PSF smearing effects. We also confirm a tight correlation between temperature and metallicity in the gas, with lower temperature plasma generally having higher metallicity.

7. CONCLUSIONS

This paper describes an application of the Markov chain Monte Carlo technique developed by us to observations with the XMM-Newton imaging instruments. We demonstrate the flexibility and power of this technique – employing Smoothed Particle Inference – via studies of three very different clusters; Abell 1689, RXJ 0658-55 and Centaurus, especially regarding the ability to determine the spatial distribution of temperature of the radiating plasma, difficult via more traditional techniques. We found evidence for cluster merger activity in all these systems, but in each case, the signature was quite distinct. The bullet of RXJ 0658-55, the remnant of a merger in Centaurus and the asymmetry of temperature in A1689 may roughly correspond to the early, middle, and late stages of cluster merging. In all cases the core of the cluster seemed relatively unaffected. Further systematic studies in temperature structure may add to our understanding of the effect of mergers on cluster properties.

We also conclude that this method will prove very powerful in the determination of cluster gas density and en-

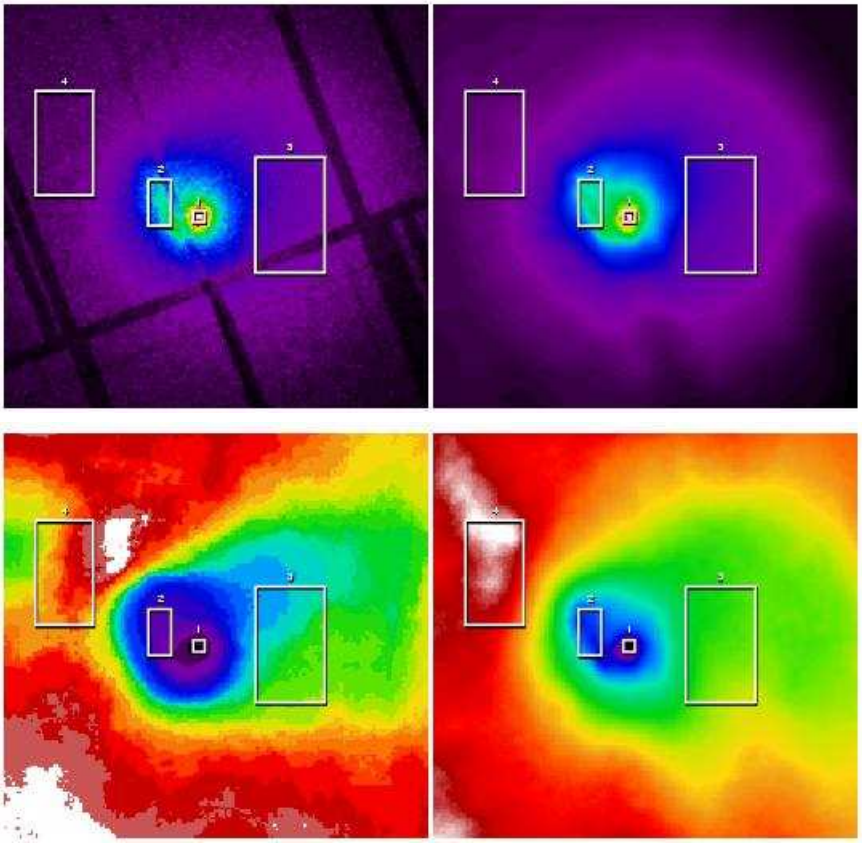

FIG. 15.— Results of analysis for the Centaurus cluster. From left to right; 1. Raw data smoothed by 4″ kernel Gaussian, 2. Luminosity reconstruction using the median of all samples at each spatial point, 3. Temperature map (0.5-6.5 keV) constructed using the mode of the distribution for all samples at each spatial point, 4. Temperature map (1.0-4.0 keV) constructed using the median of the distribution for all samples at each spatial point. All maps show a 6′ × 6′ region centered on the peak of emission.

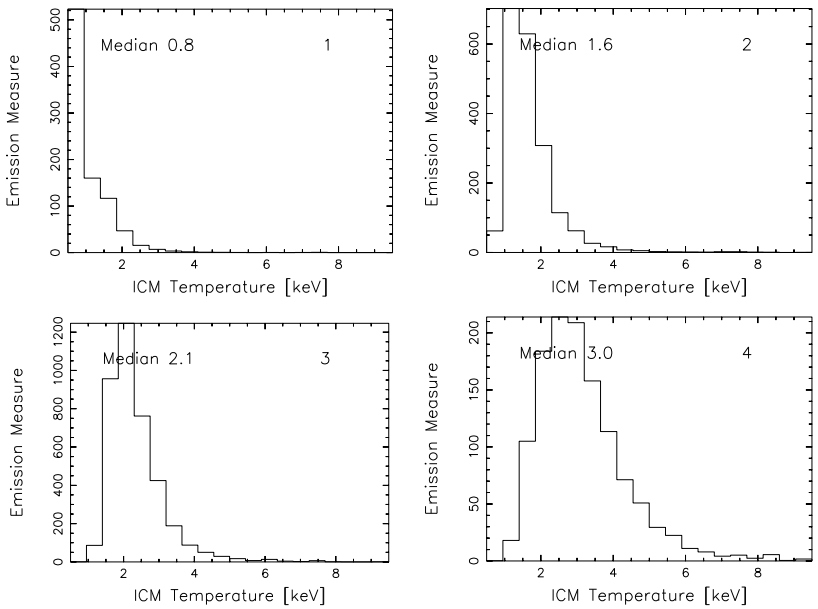

FIG. 16.— Iteration averaged distribution of temperatures for Centaurus in regions 1 through 4 also showing the median.

tropy. Since we have a multi parametric analytical model based on the Markov chain posterior, we can manipulate the smoothed particles in order to construct a three dimensional cluster model. In principle, we can choose a z-

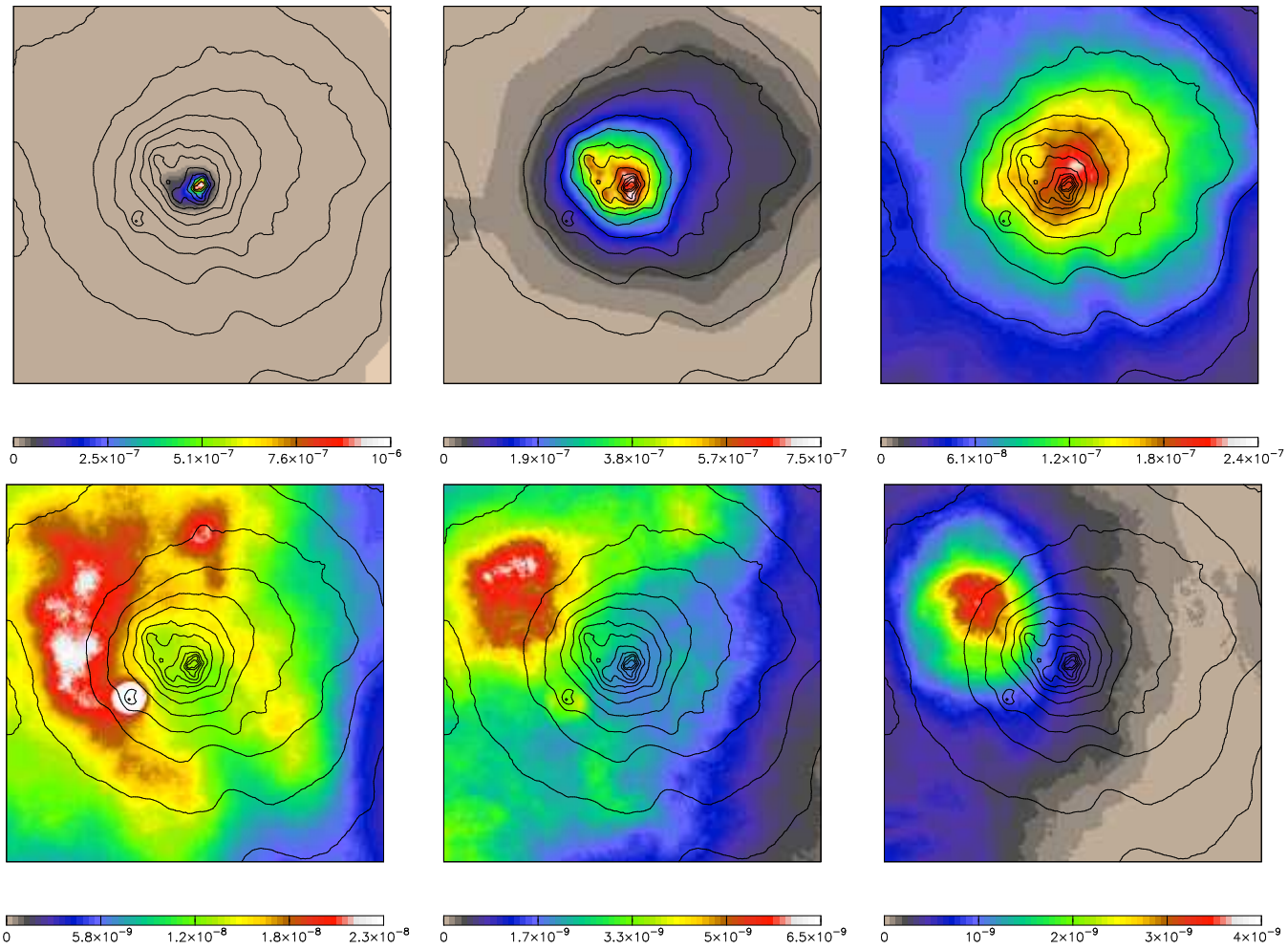

FIG. 17.— Luminosity maps of the Centaurus cluster in 0 - 1, 1 - 2, 2 - 4, 4 - 6, 6 - 8 and 8 - 10 keV temperature bands. The overlayed contours represent full band luminosity.

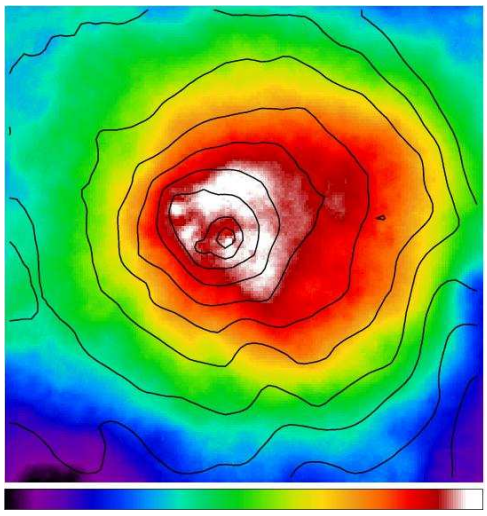

FIG. 18.— Metallicity map of the central $6' \times 6'$ region of Centaurus. The scale ranges from 0.5 to 1.0 of the Solar metallicity and contours represent luminosity.

coordinate for each particle based on some assumption of spherical symmetry. This can be done separately in bands of particle plasma temperature assuming that particles of similar temperatures exhibit the same structure as in the

two dimensional case. This will preserve the temperature gradient in the three dimensional case while preserving the two dimensional observed structure. We believe that this will be the most accurate method to determine the three dimensional spectrally resolved structure of galaxy clusters in the X-ray band.

8. ACKNOWLEDGMENTS

We acknowledge many helpful discussions on the suitability of smooth particles for modeling cluster data with Phil Marshall. Financial support for KA is provided by the Göran Gustavsson Foundation for Research in Natural Sciences and Medicine. This work was supported in part by the U.S. Department of Energy under contract number DE-AC02-76SF00515.

REFERENCES

Andersson, K. & Madejski, G. 2004, ApJ 607, 190.
Arabadjis, J. S., Bautz, M. W. & Garmire, G. P. 2002, ApJ, 572, 66
Arnaud, M. et al. 2001, A&A 365, 80.
Bradac, M. et al. 2006, ApJ, 652, 937
Broadhurst, T., Takada, M., Umetsu, K., Kong, X., Arimoto, N., Chiba, M., & Futamase, T. 2005, ApJ, 619, L143
Clowe, D., & Schneider, P. 2001, A&A, 379, 384
Clowe, D., Gonzalez, A., & Markevitch, M. 2004, ApJ, 604, 596
Clowe, D., Bradac, M., Gonzalez, A., Markevitch, M., Randall, S., Jones, C., & Zaritsky, D. 2006 ApJ, 648, 109
Dickey, J. M., & Lockman, F. J. 1990, ARA&A 28, 215.
Ehle, M., Breitfellner, M., Gonzales Riestra, R., Guainazzi, M., Loiseau, N., Rodriguez, P., Santos-Lleo, M., Schartel, N., Tomas, L., Verdugo, E., & Dahlem, M. 2006, XMM-Newton Users' Handbook, Issue 2.4, available from the XMM-Newton Science Operations Centre at http://xmm.vilspa.esa.es/external/xmm_user_support/documentation/
Fabian, A. C., Hu, E. M., Cowie, L. L., & Grindlay, J. 1981, ApJ, 248, 47
Fabian, A. C., Sanders, J. S., Taylor, G. B., & Allen, S. W. 2005, MNRAS, 360, L20
Finoguenov, A., Böhringer, H., & Zhang, Y.-Y. 2005, A & A 442, 827.
Fukazawa, Y., Ohashi, T., Fabian, A. C., Canizares, C. R., Ikebe, Y., Makishima, K., Mushotzky, R. F., & Yamashita, K. 1994, PASJ, 46, L55
Fukazawa, Y., Makishima, K., Tamura, T., Ezawa, H., Xu, H., Ikebe, Y., Kikuchi, K., & Ohashi, T. 1998, PASJ, 50, 187
Hickox, R. C., & Markevitch, M. 2006, ApJ, 645, 95
Kaastra, J. S. et al. 2003, A & A 413, 414.
Kaastra, J. S. 1992, An X-Ray Spectral Code for Optically Thin Plasmas (Internal SRON-Leiden Report, updated version 2.0)
King, L. J., Clowe, D. I., & Schneider, P. 2002, A&A, 383, 118
Kirsch, M. 2006, EPIC status of calibration and data analysis, XMM-SOC-CAL-TN-0018, available from http://xmm.vilspa.esa.es/external/xmm_sw_cal/calib/
Liang, H., Hunstead, R. W., Birkinshaw, M., & Andreani, P. 2000, ApJ, 544, 686
Liang, H., Ekers, R. D., Hunstead R.W., Falco E.E., & Shaver P. 2001, MNRAS, 328, 21
Liedahl, D. A., Osterheld, A. L., & Goldstein, W. H. 1995, ApJ, 438, L115
Lokas, E., Prada, F., Wojtak, R., Moles, M., & Gottlober, S. 2006, MNRAS, 366, L26
Lumb, D. H., EPIC Background Files, XMM-SOC-CAL-TN-0016
Markevitch, M. et al., 2000, ApJ 541, 542
Markevitch, M. et al., 2002, ApJ 567, 27
Mewe, R., Gronenschild, E. H. B. M., & van den Oord, G. H. J. 1985, A&AS, 62, 197
Mewe, R., Lemen, J. R., & van den Oord, G. H. J. 1986, A&AS, 65, 511
Miralda-Escude, J., & Babul, A. 1995, ApJ, 449, 18
Morrison, R. & McCammon, D. 1983, ApJ, 270, 119
Petrosian, V., Madejski, G., & Luli, K. 2006, ApJ, 652, 948
Peterson, J. R. et al. 2001, A & A 365, 104.
Peterson, J. R., Jernigan, J. G., & Kahn, S. M. 2004, ApJ 615, 545
Peterson, J. R., Marshall P. J., & Andersson, K. E. 2007, to appear in ApJ.
Pratt, G. W. & Arnaud, M. 2002, A & A 394, 375
Read et al. 2005, ESA-SP 604
Sanders, J. S., Fabian, A. C., Allen, S. W., & Schmidt, R. W. 2004, MNRAS 349, 952.
Sanders, J. S., & Fabian, A. C. 2006, MNRAS, 371, 1483
Tucker, W. H., Tananbaum, H., & Remillard, R. A. 1995, ApJ, 444, 532
Tucker, W., Blanco, P., Rappaport, S. et al. 1998, ApJ, 496, 5
Tyson, J. A., & Fischer, P. 1995, ApJ, 446, L55
Zhang, Y.-Y., Finoguenov, A., Böhringer, H., Ikebe, Y., Matsushita, K., & Schuecker, P. 2004, A & A 413, 49.